Size-Specific Magnetic Configurations in Electrodeposited Epitaxial Iron Nanocuboids: From Landau Pattern to Vortex and Single Domain States

Shanshan Guo, Mara Henschel, Daniel Wolf, Darius Pohl, Axel Lubk, Thomas Blon, Volker Neu, Karin Leistner

Size-specific magnetic configurations in electrodeposited epitaxial iron nanocuboids: From Landau pattern to vortex and single domain states

Shanshan Guo,[1,] Mara Henschel,[1] Daniel Wolf,[1] Darius Pohl,[2] Axel Lubk,[1] Thomas Blon,[3] Volker Neu,[1] Karin Leistner[1,4]*

[1] Leibniz IFW Dresden, 01069 Dresden, Germany

[2] Dresden Center for Nanoanalysis, Center for Advancing Electronics Dresden, TU Dresden, 01069 Dresden, Germany

[3] Université de Toulouse, INSA-CNRS-UPS, LPCNO,135 Av. Rangueil, 31077 Toulouse, France

[4] Electrochemical Sensors and Energy storage, Faculty of Natural Sciences, Institute of Chemistry, TU Chemnitz, 09111 Chemnitz, Germany

KEYWORDS: nano-electrodeposition, progressive nucleation, iron nanocuboids, magnetic configuration, Landau pattern, vortex, single domain

ABSTRACT: As the size of magnetic devices continuously decreases, the creation of three-dimensional nanomagnets and the understanding of their magnetic configurations become increasingly important for modern applications. Here, by progressive nucleation during epitaxial nano-electrodeposition, we synthesize single-crystal iron nanocuboids with sizes ranging 10 nm to 200 nm on one sample. The size-dependent magnetic configurations of these nanocuboids are studied by quantitative magnetic force microscopy and electron holography. In conjunction, a

"magnetic configuration versus size" phase diagram is established via micromagnetic simulations. Both experiment and theory reveal a sequential transition from Landau pattern to vortex and finally single domain when decreasing the nanocuboid size. The combinatorial-like approach leads to a quantitative understanding of the magnetic configurations of the nanomagnets in a broad size range. It can be transferred to other materials and shapes, and thereby presents an advanced route to enrich the material library for future nanodevice design.

Introduction

The extension of nanomagnetism into three dimensions (3D) entails the emergence of unprecedented magnetic textures, with high application potential for modern devices.[1] For instance, the single domain, exhibiting a uniform distribution of moments, is typically optimized for applications requiring hard magnetic behavior, such as hard disk drives.[2, 3] A vortex state, in which the external spins circulate to achieve flux closure, whereas the core spins turn toward the surface normal,[4, 5] is exploited in medical biology such as drug delivery to minimize the stray field around the particle and thus prevent magnetic aggregation.[5] And, the multidomain configuration is now explored in magnetic nanowires to benefit from domain-wall motion for magnetic racetrack memories.[6-8]

Magnetic configurations strongly depend on the geometry and the size of the magnetic nanoobjects.[1, 5, 9, 10] Therefore, engineering the geometry of nanomagnets has created a series of versatile magnetic textures, e.g., vortices in magnetic spheres,[11, 12] skyrmions in multi-layered elements with symmetry breaking,[13-16] as well as domain walls in nanowires.[17-19] Besides, transition between different magnetic configurations can also be obtained through controlling the size of the nanoobjects even of simplest geometries.[4] Most studies on size-dependent magnetic configurations deal with patterned elements with nanometer scale thickness and lateral dimensions

in the range of several hundred nanometers to micrometers.[9, 20, 21] These nanomagnets usually exhibit small aspect ratio (height/width), and the transition between vortex and single domain occurs at lateral sizes of more than hundred nanometers.[3, 10, 22] To fully exploit the advantages of size-dependent control of magnetic configurations in future nanodevices, nanoobjects of smaller size must be studied. The increase of the aspect ratio is one promising route toward stabilization of versatile magnetic states at much smaller lateral dimensions.[23, 24] The advent of the epitaxial nano-electrodeposition method,[25] an advanced electrochemical synthesis technique capable of growing defined single-crystal nanoobjects with high aspect ratio directly on a substrate, renders the expansion of 3D nanomagnetism into lower dimensions possible. In addition, the nucleation and growth mode in electrodeposition can be controlled by controlling the deposition potential and by applying pulse procedures. This way, one can switch between the instantaneous nucleation, where the density of nuclei keeps constant over time, and the progressive nucleation, where the density of nuclei increases linearly with time.[26-30] In the progressive case, new nuclei continue to be nucleated while their siblings grow larger as time advances.[26] Thus, nanoobjects with a wide size distribution can be produced, opening up an effective avenue towards nanomaterial synthesis for size-dependent magnetic configuration studies.

Here, we take advantage of the progressive nucleation during epitaxial nano-electrodeposition to synthesize single-crystal iron nanocuboids of sizes ranging from 10 nm to 200 nm. We use this one-step synthesis as a combinatorial approach to study the size-dependent magnetic configurations directly on one sample. To establish the "magnetic configurations vs size" phase diagram, the size limit separating each state must be determined. However, most magnetic characterization techniques are optimized to probe planar systems or are only suitable for a certain size range.[1] Their extension to the study of 3D nanomagnets with complex vectoral spin textures

and geometries, is far from trivial, and requires new methodologies or multi-technique approaches.[1] We combine micromagnetic simulations with quantitative magnetic force microscopy (qMFM) and electron holography (EH) to in detail reveal the size-dependent magnetic configurations. When reducing the cuboid size, a transition from Landau pattern to vortex and finally single domain was theoretically and experimentally resolved. Our study enriches the 3D nanomagnetic material library to impact areas such as sensing, data storage, nanoelectronics and medical biology.

Results and Discussion

To obtain isolated iron nanocuboids with a wide size distribution, the epitaxial electro-deposition was carried out in a progressive nucleation mode on the GaAs (001) substrate. Epitaxial growth was promoted by using the "hot" plating technique, i.e., the sample is immersed in the electrolyte as working electrode while a high cathodic potential pulse (-5 V for < 1 s) is applied to it. This procedure enforces a strong hydrogen evolution reaction and thereby avoids blocking of the GaAs surface by adsorbed hydrogen.[31] Progressive nucleation then takes place in the subsequent galvanostatic deposition with a current density of 1 mA/cm^2 for 10 s. The fabrication details can be found in Methods (Supporting Information) and in previous publications.[25, 31] The microstructure of the as-prepared sample was investigated by scanning electron microscopy (SEM), atomic force microscopy (AFM), transmission electron microscopy (TEM) and electron energy-loss spectroscopy (EELS). Figure 1a reveals that the separately dispersed iron cuboids are aligned with a specific crystallographic orientation on the GaAs substrate, which evidences epitaxial growth. More specifically, the edge and the diagonal of the cuboids orient along the [100] and [110] GaAs-substrate directions, respectively. Statistical analysis of the cuboid size (edge length) determined by SEM, discloses a log-normal size distribution (Figure 1b), which is expected for

the progressive nucleation mode,[29] from around 10 nm to 200 nm. Further size analysis by incorporating SEM with AFM profile reveals an average aspect ratio (height/width) of 0.46. Cross-sectional TEM analysis (Figure 1c and S1a) shows the cuboids with a rectangular cross-section. EELS mapping (Figure 1d) identifies the elemental distribution of Ga, Fe and O, respectively. The sharp surface of the GaAs substrate can be seen from the Ga-L mapping, which discloses that interdiffusion between Fe cuboid and GaAs substrate does not happen during the room-temperature electrodeposition process. Besides, a thin oxide shell covers the iron core, as disclosed by the Fe-L and the O-K mapping. High-resolution TEM (HRTEM) investigations (Figure 1 e-h) further reveal the epitaxial relation of Fe(100)[001] // GaAs(100)[001], which is evidenced by the Fast-Fourier transform (FFT) patterns (Figure 1f,g) extracted in the iron-cuboid core and GaAs substrate, respectively. A nearly undisturbed Fe/GaAs interface is shown in Figure 1h.

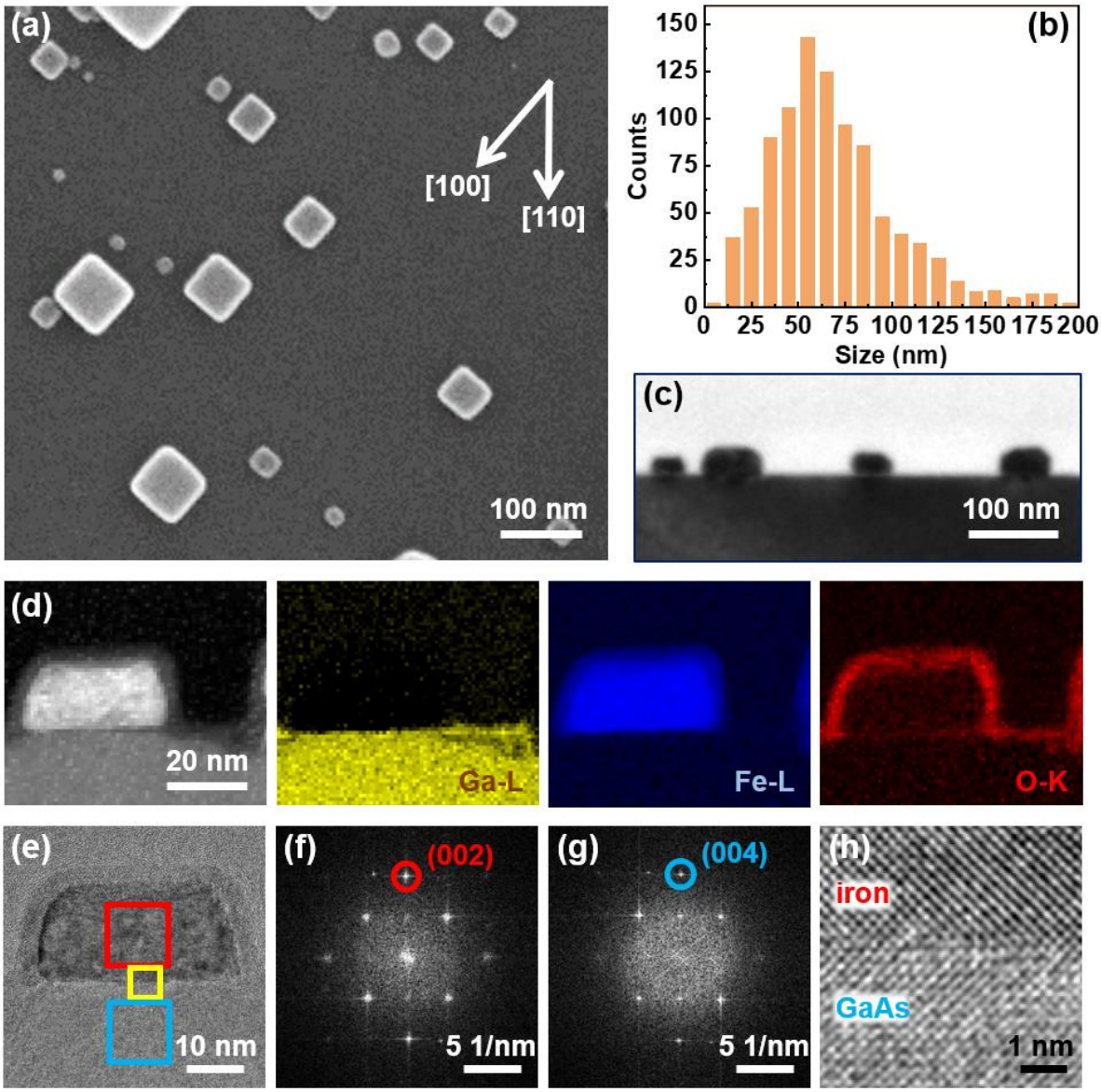

Figure 1. Microstructure of the electrodeposited iron nanocuboids. (a) SEM image showing isolated iron cuboids with different sizes. (b) Size distribution of iron cuboids. (c) Cross-sectional bright field TEM image. (d) High-angle-annular-dark-field TEM image and EELS mapping of Ga, Fe and O in iron cuboid. (e) HRTEM image with marked areas for Fast-Fourier transforms of the iron cuboid (f) and the GaAs substrate (g) and a zoom at the interface region (h).

To get an overview of the magnetic configurations of the iron cuboids, we at first conducted a qualitative MFM study on the as-prepared sample. Figure 2a shows an MFM phase image. Its corresponding topography is shown in Figure S2. From the magnetic-phase contrast (Figure 2a), the existence of different magnetic configurations for nanocuboids with different size can already

be deduced, comparing e.g., the phase contrasts of the three cuboids marked with i, ii and iii. The cuboid i (46 nm in edge length), exhibits a dark-white halfmoon contrast, implying a dipolar single-domain state. The homogenous white contrast inside the larger cuboid ii (~ 69 nm) is typical for a vortex-like configuration. The cross-shaped contrast on the largest one (cuboid iii, 115 nm) is later confirmed to be a Landau state. Besides, we note that black contours surround some cuboids, e.g., the cuboid ii. The MFM phase signal of 3D nanoparticles has to be carefully interpreted, as topographic fluctuations always mix artefacts into the magnetic-phase signal. To decide whether phase contrasts are of magnetic origin or artefacts, the magnetization of the MFM tip was reversed to scan the same area. Figure 2b and 2c present the phase signal obtained with the same magnetic tip but once with downward magnetization and once with upward magnetization, respectively. Comparing the resulting phase contrast in Figure 2b, c, we see that the phase contrast inside each cuboid reversed from white to black (upper cuboid), or from black to white (lower cuboid), while the black contours of the two cuboids keep unchanged. Thus, it is confirmed that the interior phase contrast is the magnetic signal, while the black contour is the nonmagnetic artefact. Further, we assessed the stability of the magnetic configurations by comparing the phase signal of the same cuboids in pristine state and after application of a magnetic field. Figure 2d and 2e show the phase signal of one cuboid (~54 nm) captured at its as-grown state and after in-plane magnetizing with a 3 T magnetic field applied along the [100] direction, respectively. We found that in this case, the vortex-like state is stable. In contrast, the remnant magnetic state of cuboid of 46 nm size can be switched from a vortex-like state (Figure 2f) to single-domain state (Figure 2g) by applying a 3 T in-plane magnetic field along the [100] direction, implying a possible metastable state. The explanation of this metastable state is further discussed later in the manuscript.

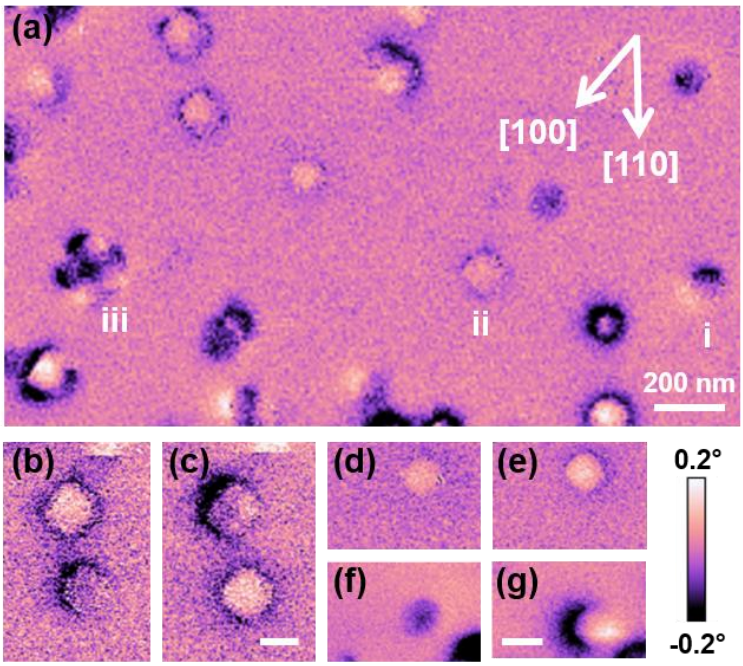

Figure 2. Qualitative MFM overview study of the iron cuboids. (a) MFM phase image showing isolated iron cuboids with different magnetic configurations, e.g., cuboids marked with i, ii, iii, respectively. Magnetic phase image captured with a magnetic tip with (b) downward magnetization and (c) upward magnetization. MFM phase images showing vortex-like states of one cuboid (~54 nm) at (d) the as-grown state and (e) remnant state after in-plane magnetizing along the edge. (f) Vortex-like state and (g) single-domain state of an iron cuboid (~46 nm) captured after in-plane magnetizing along the edge. Scale bar of b-g: 100 nm. Intensity bar of a-g shown at the bottom right corner.

To predict the size limit separating each magnetic configuration, micromagnetic simulations were performed using the 3D OOMMF package.[32] Results presented in Figure 3 were obtained for Fe cuboids with <100> crystal directions along the cuboid edges (as experimentally confirmed in Figure 1). More details about the micromagnetic simulations can be found in the Supporting Information. The resulting energies of ground states were calculated for different cuboid sizes and shown in Figure 3a as blue circle, purple square, upward triangle and downward triangle for demagnetizing energy density, exchange energy density, anisotropy energy density and total energy density, respectively. With uniform distribution of moments, the single-domain state (Figure 3b) minimizes the exchange energy and anisotropy energy for small cuboid sizes but at the expense of the demagnetization energy due to the presence of surface magnetic charges where

magnetization is normal to the surface. With increasing cuboid size, sharp magnetic transition occurs at 42 nm, that is, around 18 times of the Fe exchange length (l_{ex}^{Fe} = 2.4 nm). Then, the vortex state (Figure 3c),[4, 33] in which external spins rotate to achieve a flux closure, whereas the core spins tilt out-of-plane, becomes energetically favorable. This closed-flux configuration avoids most of the demagnetization energy at the expense of a large exchange energy. Upon further increasing the size, a continuous transition from the vortex to a Landau pattern (i.e., flux-closure domain state, Figure 3d) is expected. Both the vortex and the Landau pattern are largely stray-field-free. In the flux-closed Landau pattern,[33, 34] the magnetic moments parallel to the cubic anisotropy axis in the domains save anisotropy energy despite extra wall energy.

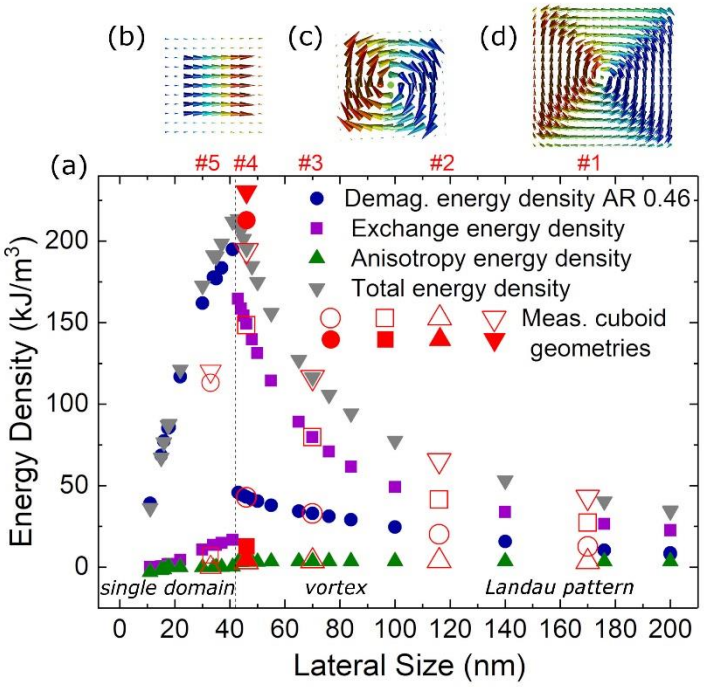

Figure 3. Theoretical "magnetic configuration versus size" phase diagram. (a) Calculated magnetic energy densities of magnetic ground states of iron nanocuboids (including a 4 nm Fe_3O_4 shell) as a function of the size of cuboids of aspect ratio 0.46. Blue circle: demagnetizing energy density, purple square: exchange energy density, upward triangle: magnetocrystalline anisotropy energy density, downward triangle: total energy density. Open red symbols correspond to the calculations for the dimensions of experimentally measured cuboids, which are referenced with numbers at the upper *x* axis (Cuboid #5 is displayed with 'averaged' lateral size of 33 nm. See Supporting Information). Filled red symbols correspond to the calculations for a metastable single-domain state of cuboid #4 (see text following). Top views of simulated magnetic configurations: (b) single domain, (c) vortex and (d) Landau pattern.

Experimentally, we evidenced the sequential size-dependent magnetic transition among Landau pattern, vortex and single domain through a qMFM technique. qMFM allows validating the 3D magnetization pattern of a nanomagnet from the common 2D MFM data. The technique is based on (i) a quantitative MFM measurement[35-38] of the iron cuboids with a calibrated tip,[39] (ii) a micromagnetic calculation of the expected total magnetic charges at the sample surface, and (iii) a quantitative comparison of the thus expected MFM contrast with the measured data. By using the depth sensitivity of MFM and by applying a quantitative contrast analysis, we are able to verify the inhomogeneous magnetization state of the individual iron cuboid. Details of qMFM measurements and analysis procedures, including the treatment of the corrugated sample surface, can be found in Methods (Supporting Information).

For the experimental characterization by qMFM, we selected four representative cuboids and numbered them with #1, #2, #3, and #4, respectively, to align them with the magnetic phase diagram predicted in Figure 3. Topography of the four selected cuboids is shown in Figure S3. Figure 4a-#1 displays the extracted effective surface pattern of cuboid #1 (edge length: $x = y = 170$ nm, height: $z = 64$ nm) as derived from the Landau pattern visible in the magnetization structure (Figure 3d). The magnetic vortex in the cuboid center relates to a magnetic pole with positive charge, and the 90° Néel walls separating the 4 triangular domains result in two shifted cross-like features with opposite polarity. The convolution with the tip transfer function (TTF) presents the quantitative MFM contrast expected for cuboid #1 (Figure 4b-#1). The contrast is confined to the region of the cuboid. Due to the finite size of the TTF profile (FWHM = 90 nm, Figure S4c), cross structure is obviously blurred, but nevertheless clearly visible. This calculated contrast resembles well the measured MFM signal (Figure 4c-#1), except for the stronger contrast at the cuboid rim, discussed already as an artefact of the tip scanning the cuboid contour (Figure 2b, c). Note that the

measured image (Figure 4c) is rotated by 45° with respect to the measurement direction in order to match the cuboid orientation of the micromagnetic simulation. If we restrict to a region inside the cuboid (avoiding the rim), we do observe a very good quantitative agreement (24% normalized root mean square error (RMS)) of measured and simulated MFM contrast in the phase profile (Figure 4d-#1), confirming not only qualitatively the presence of the Landau structure, but also its correct micromagnetic description. The error has to be judged against a typical expanded uncertainty of about 16% for the TTF reconstruction[40] and further uncertainties, especially originating from the very weak interaction with the nanoscale cuboid and the mentioned topographic artefact. The smaller cuboid #2 ($x = y = 116$ nm, $z = 54$ nm) shows very similar behavior. Also here, the Landau magnetization structure is obvious from the cross-shaped contrast in the effective magnetic surface map (Figure 4a-#2). Again, calculated MFM contrast match the measured data, both qualitatively and quantitatively (25% RMS) (Figure 4(b-d)-#2).

The situation changes when the cuboids become even smaller. For cuboid #3 ($x = y = 69$ nm, $z = 32$ nm), the character of the magnetization structure is increasingly dominated by the magnetization vortex, and due to missing divergences in regions of continuous flux closure, magnetic charges are now confined to the vortex core in the cuboid center and to the corners (Figure 4a-#3). Furthermore, the unavoidable signal broadening by the imaging process (TTF FWHM = 90 nm, Figure S4c) doesn't allow resolving these differences, despite a reduced tip-sample distance of 50 nm. Hence, the calculated MFM image (Figure 4b-#3) reduces to a weak contrast on the position of the cuboid, as also imaged in the experiment (Figure 4c-#3). Again, the contrast is also quantitatively well described (18% RMS) by the qMFM analysis (Figure 4d-#3).

These experimental configurations (Figure 4) have been compared with theoretical results of the micromagnetic simulations (Figure 3). The open symbols in the phase diagram (Figure 3)

illustrate the energy densities for the simulated and experimentally confirmed ground states of cuboid #1, #2 and #3. A very good agreement between simulated magnetic configurations and experimental maps is obtained. Furthermore, the two aforementioned magnetic configurations, i.e., the Landau pattern and the vortex state, remain stable after applying a 3 T in-plane magnetic field along the cuboid edge. However, for cuboid #4 ($x = y = 46$ nm, $z = 20$ nm), a 3 T in-plane magnetic field can lead to either single domain (Figure 4(a-d)-#4) or vortex states (Figure S6), implying a metastable state. Figure 4(a-d)-#4 summarizes the analysis for cuboid #4 showing single-domain configuration at remanence after saturating along the [100] direction. The difference to the vortex state is clearly visible in a contrast modulation across the cuboid (bright-dark contrast), both in the simulated (Figure 4b-#4) and the experimental MFM (Figure 4c-#4). Indeed, a metastable state for cuboid #4 is theoretically supported, as the size of 46 nm is close to the sharp phase boundary between a vortex state and an in-plane single-domain state (filled symbols in Figure 3a). The total energy density of the vortex state (ground state) and the single-domain state (metastable state) for this size are very similar.

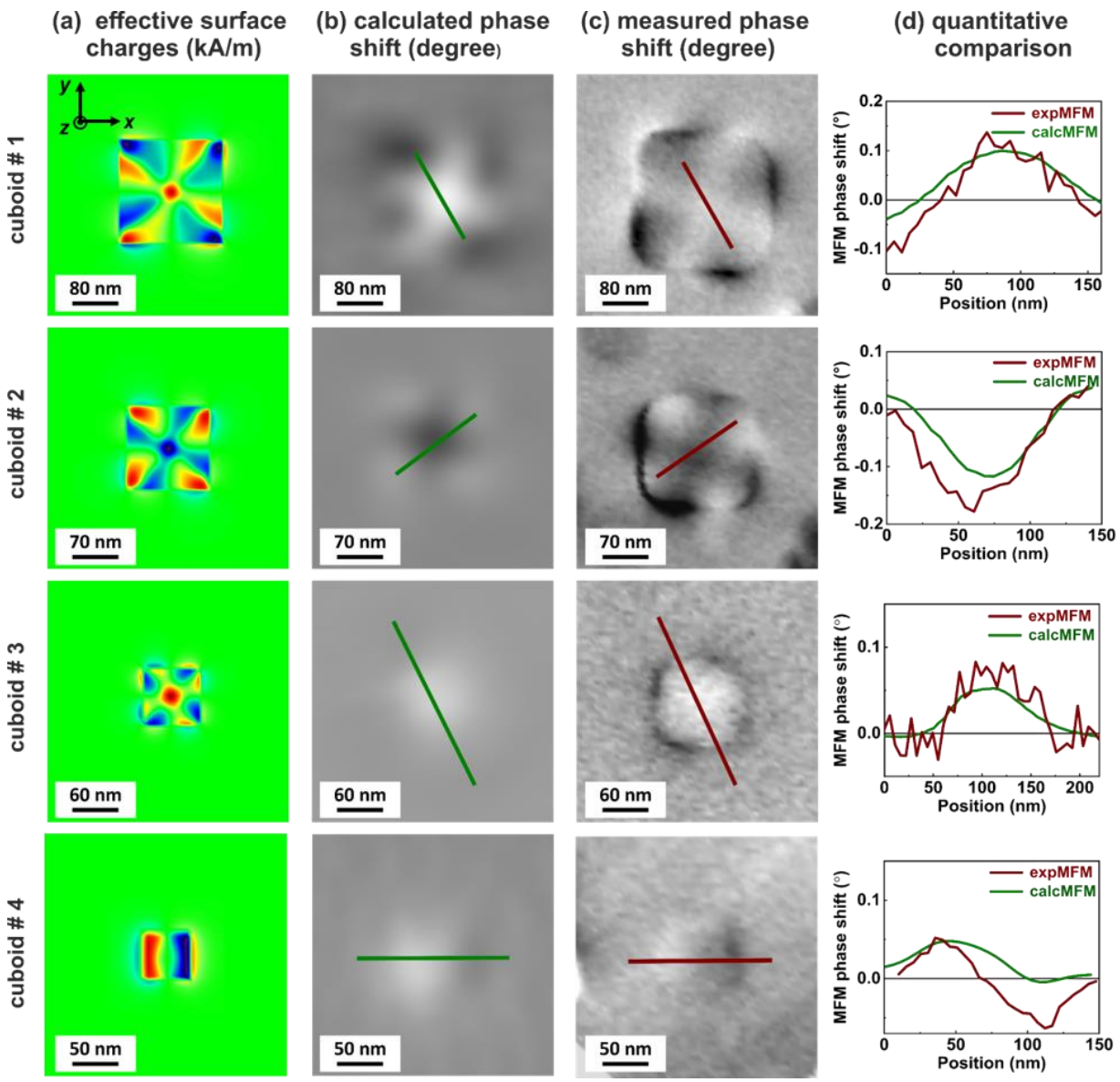

Figure 4. Quantitative comparison between calculated and measured MFM contrast for Fe cuboids with decreasing size. The 4 columns show (from left to right) (a) the effective magnetic surface charge tracing the upper surface of the cuboid, (b) the expected MFM contrast by convolving the effective surface charge with the TTF, (c) the measured MFM contrast, (d) MFM contrast profiles through (b) and (c) at the marked position across the cuboid #1 ($x = y = 170$ nm, $z = 64$ nm), cuboid 2 ($x = y = 116$ nm, $z = 54$ nm), cuboid #3 ($x = y = 69$ nm, $z = 32$ nm), cuboid #4 ($x = y = 46$ nm, $z = 20$ nm), respectively.

As previously discussed, the resolution of MFM limits further exploration of magnetic configurations for smaller iron cuboids (below 40 nm). Therefore, off-axis EH[41-43] has been used to resolve the magnetic configurations of smaller iron cuboids. EH is an interferometric TEM method, which allows to reconstruct the Aharonov-Bohm phase shift of the electrons transmitted

through the specimen with a spatial resolution of a few nanometers under magnetic field-free conditions in so-called Lorentz mode. The EH measurement and analysis details are provided in Methods and Figure S7 (Supporting Information).

Figure 5 shows experimental and simulated phase images of an iron cuboid with a lateral size below 40 nm (cuboid #5). In these images, the electrostatic contribution φ_{el} to the phase image is displayed as grayscale depicting the projected morphology, whereas the magnetic contribution φ_{mag} is superimposed as red isolines. The latter is generated by calculating $\cos(50\times\varphi_{mag})$, which means that the difference between red and dark-red isolines is $\pi/50$. Indeed, the magnetic equi-phase lines are proportional to the projected field lines of the in-plane magnetic flux density B. For example, the highest projected magnetic flux density within the iron cuboid corresponds to a projected B-field of 20 Tnm. The experimentally observed cuboid shows uniformly magnetized single-domain state, including the characteristic return flux of an isolated magnetic dipole. The lines of projected magnetic field indicate that the magnetization direction of the cuboid lies in the plane of the specimen, parallel to the cuboid edge ([100] crystallographic direction), consistent with shape and magnetocrystalline anisotropies dominating the magnetic state of the crystal. For comparison with the experimental phase map, a phase image was calculated from the micromagnetic simulation of an iron nanocuboid supporting a single-domain state (Figure 3b) using the Aharonov-Bohm relation,[44] as shown in Figure 5b. A very good quantitative agreement between experimental and calculated phase map, visible through the same density of the red field lines within the cuboid, was obtained for the cuboid dimensions of 38 nm (y), 19 nm (z) and 28 nm (x), as well as including a 4 nm thick oxide layer (Figure 1d).

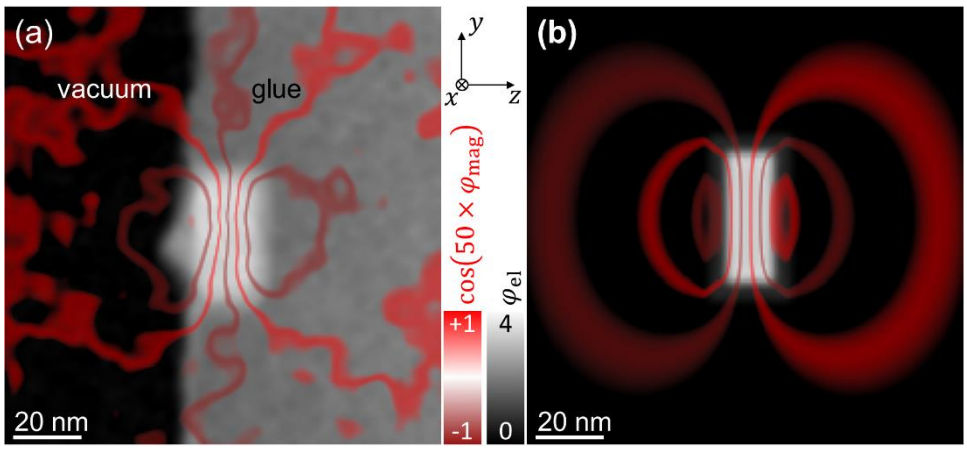

Figure 5. Phase mapping using off-axis EH of the isolated Fe cuboid #5 with a lateral size below 40 nm. (a) Experimental electric phase image (grayscale) superimposed by red isolines of the magnetic phase shift, which correspond to the projected field lines of the magnetic induction. (b) Calculated magnetic phase map from micromagnetic simulation of cuboid #5 displayed in the same way as (a).

Conclusions

By taking advantage of progressive nucleation during epitaxial nano-electrodeposition, we synthesized single-crystal iron nanocuboids of sizes ranging from 10 nm to 200 nm on one sample. With this combinatorial approach, a size-dependent magnetic phase diagram for iron nanocuboids was established experimentally and theoretically through the combination of qMFM, EH and micromagnetic simulations. With size decreasing, a sequence of Landau pattern, vortex, and single domain was theoretically and experimentally resolved. With this, our study enriches the 3D nanomagnetic material library. The combinatorial methodology based on epitaxial nano-electrodeposition can also be transferred to other material systems, such as Co, Ni, Fe/Ni alloy.[45-47] In the future, magnetic nanodevices demanding specific magnetic configurations could be further engineered by growing nanocrystals with specific size through a nucleation-mode control, i.e., the change from progressive nucleation to instantaneous nucleation.[26] Our study can impact both the fundamental knowledge advance and the perspective engineering possibilities in areas such as sensing, data storage, nanoelectronics and medical biology.

ASSOCIATED CONTENT

Supporting Information

Supporting Information: methods (including sample synthesis, micromagnetic simulations, quantitative MFM measurements, TTF construction, quantitative MFM analysis, and electron holography measurements,), cross-sectional TEM images, topography image scanned with AFM, SEM images of the four selected iron cuboids shown in Figure 4, tip calibration via Co/Pt reference sample, quantitative cuboid analysis, cuboid at a metastable state showing vortex configuration, a TEM lamella used for electron holography measurements.

AUTHOR INFORMATION

Corresponding Author

*Shanshan Guo - Leibniz IFW Dresden, Dresden 01069, Germany; Email: s.guo@ifw-dresden.de

Author Contributions

K.L. conceived the idea, M.H. fabricated the iron cuboids samples, S.G. performed the qMFM measurements, V.N. calculated the qMFM results, T.B. carried out the micromagnetic simulations, D.W. and A.L. performed electron holography characterization and analysis, D.P. did the TEM characterization. S.G. wrote the manuscript with inputs from V.N., T.B., D.W., A.L. and K.L., and all authors contributed to the discussion of the results.

Notes

The authors declare no competing financial interest.

ACKNOWLEDGMENT

We acknowledge S. Neitsch for technical help of electrodeposition, and T. Sturm and A. Pöhl for FIB preparation of the TEM lamellas (all at Leibniz IFW Dresden). This work is partly supported by the German Science Foundation (DFG) under project 400178764. D.W. and A.L. have received funding from the European Research Council (ERC) under the Horizon 2020 Research and Innovation Program of the European Union (grant agreement number 715620).

REFERENCES

1. Fernandez-Pacheco, A.; Streubel, R.; Fruchart, O.; Hertel, R.; Fischer, P.; Cowburn, R. P. Three-Dimensional Nanomagnetism. *Nat. Commun.* **2017,** *8*, 15756.
2. Terris, B. D.; Thomson, T. Nanofabricated and Self-Assembled Magnetic Structures as Data Storage Media. *J. Phys. D: Appl. Phys.* **2005,** *38*, R199-R222.
3. Yamasaki, A.; Wulfhekel, W.; Hertel, R.; Suga, S.; Kirschner, J. Direct Observation of the Single-Domain Limit of Fe Nanomagnets by Spin-Polarized Scanning Tunneling Spectroscopy. *Phys. Rev. Lett.* **2003,** *91*, 127201.
4. Gatel, C.; Bonilla, F. J.; Meffre, A.; Snoeck, E.; Warot-Fonrose, B.; Chaudret, B.; Lacroix, L. M.; Blon, T. Size-Specific Spin Configurations in Single Iron Nanomagnet: From Flower to Exotic Vortices. *Nano Lett.* **2015,** *15*, 6952-6957.
5. Lewis, G. R.; Loudon, J. C.; Tovey, R.; Chen, Y. H.; Roberts, A. P.; Harrison, R. J.; Midgley, P. A.; Ringe, E. Magnetic Vortex States in Toroidal Iron Oxide Nanoparticles: Combining Micromagnetics with Tomography. *Nano Lett.* **2020,** *20*, 7405-7412.

6. Parkin, S. S. P.; Hayashi, M.; Thomas, L. Magnetic Domain-Wall Racetrack Memory. *Science* **2008,** *320*, 190-194.

7. Al Bahri, M.; Borie, B.; Jin, T. L.; Sbiaa, R.; Klaui, M.; Piramanayagam, S. N. Staggered Magnetic Nanowire Devices for Effective Domain-Wall Pinning in Racetrack Memory. *Phys Rev Appl* **2019,** *11*, 024023.

8. Honda, S.; Kaiya, Y.; Itoh, H.; Ohsawa, T. Magnetic Domain With Straight Domain Walls Passing Through a Ferromagnetic Insulator for a Continuously Looped Racetrack Memory. *IEEE Trans. Magn.* **2021,** *57*, 4300305.

9. Wren, T.; Gribkov, B.; Petrashov, V.; Kazakova, O. Phase Diagram of Magnetic States in Nickel Submicron Disks. *J. Appl. Phys.* **2015,** *118*, 023906.

10. T. Shinjo, T. O., R. Hassdorf, K. Shigeto, T. Ono. Magnetic Vortex Core Observation in Circular Dots of Permalloy. *Science* **2000,** *289*, 930-932.

11. Kim, S. K.; Yoo, M. W.; Lee, J.; Lee, J. H.; Kim, M. K. Resonant Vortex-Core Reversal in Magnetic Nano-Spheres as Robust Mechanism of Efficient Energy Absorption and Emission. *Sci. Rep.* **2016,** *6*, 31513.

12. Kim, M.-K.; Sim, J.; Lee, J.-H.; Kim, S.-K. Tunable Specific-Loss Power of Magnetic Nano-Spheres in Vortex State for High-Efficiency Hyperthermia Bio-Applications: A Theoretical and Simulation Study. *J. Appl. Phys.* **2019,** *125*, 063901.

13. Song, K. M.; Jeong, J.-S.; Pan, B.; Zhang, X.; Xia, J.; Cha, S.; Park, T.-E.; Kim, K.; Finizio, S.; Raabe, J.; Chang, J.; Zhou, Y.; Zhao, W.; Kang, W.; Ju, H.; Woo, S. Skyrmion-Based Artificial Synapses for Neuromorphic Computing. *Nat. Electron.* **2020,** *3*, 148-155.

14. Lo Conte, R.; Nandy, A. K.; Chen, G.; Fernandes Cauduro, A. L.; Maity, A.; Ophus, C.; Chen, Z.; N'Diaye, A. T.; Liu, K.; Schmid, A. K.; Wiesendanger, R. Tuning the Properties of Zero-

Field Room Temperature Ferromagnetic Skyrmions by Interlayer Exchange Coupling. *Nano Lett.* **2020,** *20*, 4739-4747.

15. Yu, G.; Jenkins, A.; Ma, X.; Razavi, S. A.; He, C.; Yin, G.; Shao, Q.; He, Q. L.; Wu, H.; Li, W.; Jiang, W.; Han, X.; Li, X.; Bleszynski Jayich, A. C.; Amiri, P. K.; Wang, K. L. Room-Temperature Skyrmions in an Antiferromagnet-Based Heterostructure. *Nano Lett.* **2018,** *18*, 980-986.
16. Srivastava, T.; Schott, M.; Juge, R.; Krizakova, V.; Belmeguenai, M.; Roussigne, Y.; Bernand-Mantel, A.; Ranno, L.; Pizzini, S.; Cherif, S. M.; Stashkevich, A.; Auffret, S.; Boulle, O.; Gaudin, G.; Chshiev, M.; Baraduc, C.; Bea, H. Large-Voltage Tuning of Dzyaloshinskii-Moriya Interactions: A Route toward Dynamic Control of Skyrmion Chirality. *Nano Lett.* **2018,** *18*, 4871-4877.
17. Parkin, S. S.; Hayashi, M.; Thomas, L. Magnetic Domain-Wall Racetrack Memory. *Science* **2008,** *320*, 190-194.
18. Ferguson, C. A.; MacLaren, D. A.; McVitie, S. Metastable Magnetic Domain Walls in Cylindrical Nanowires. *J. Magn. Magn. Mater.* **2015,** *381*, 457-462.
19. Ivanov, Y. P.; Chuvilin, A.; Lopatin, S.; Kosel, J. Modulated Magnetic Nanowires for Controlling Domain Wall Motion: Toward 3D Magnetic Memories. *ACS Nano* **2016,** *10*, 5326-5332.
20. Pulwey, R.; Zölfl, M.; Bayreuther, G.; Weiss, D. Magnetic Domains in Epitaxial Nanomagnets with Uniaxial or Fourfold Crystal Anisotropy. *J. Appl. Phys.* **2002,** *91*, 7995-7997.
21. Ghidini, M.; Mansell, R.; Pellicelli, R.; Pesquera, D.; Nair, B.; Moya, X.; Farokhipoor, S.; Maccherozzi, F.; Barnes, C. H. W.; Cowburn, R. P.; Dhesi, S. S.; Mathur, N. D. Voltage-Driven Annihilation and Creation of Magnetic Vortices in Ni Discs. *Nanoscale* **2020,** *12*, 5652-5657.

22. Cowburn, R. P.; Koltsov, D.; Adeyeye, A.; Welland, M.; Tricker, D. Single-Domain Circular Nanomagnets. *Phys. Rev. Lett.* **1999,** *83*, 1042-1045.

23. Ross, C. A.; Hwang, M.; Shima, M.; Cheng, J. Y.; Farhoud, M.; Savas, T. A.; Smith, H. I.; Schwarzacher, W.; Ross, F. M.; Redjdal, M.; Humphrey, F. B. Micromagnetic Behavior of Electrodeposited Cylinder Arrays. *Phys. Rev. B* **2002,** *65*, 144417.

24. Bonilla, F. J.; Lacroix, L. M.; Blon, T. Magnetic Ground States in Nanocuboids of Cubic Magnetocrystalline Anisotropy. *J. Magn. Magn. Mater.* **2017,** *428*, 394-400.

25. Leistner, K.; Yang, M.; Damm, C.; Oswald, S.; Petr, A.; Kataev, V.; Nielsch, K.; Kavanagh, K. L. Aligned Cuboid Iron Nanoparticles by Epitaxial Electrodeposition. *Nanoscale* **2017,** *9*, 5315-5322.

26. Guo, L.; Oskam, G.; Radisic, A.; Hoffmann, P. M.; Searson, P. C. Island Growth in Electrodeposition. *J. Phys. D: Appl. Phys.* **2011,** *44*, 443001.

27. Pei, A.; Zheng, G.; Shi, F.; Li, Y.; Cui, Y. Nanoscale Nucleation and Growth of Electrodeposited Lithium Metal. *Nano Lett.* **2017,** *17*, 1132-1139.

28. Youbi, B.; Lghazi, Y.; Ait Himi, M.; Bimaghra, I. Nucleation and Growth Mechanism of Tellurium Electrodeposited on Tin-Doped Indium Oxide Substrate. *J. Appl. Electrochem.* **2019,** *50*, 159-168.

29. Teran, A. V.; Bill, A.; Bergmann, R. B. Time-Evolution of Grain Size Distributions in Random Nucleation and Growth Crystallization Processes. *Phys. Rev. B* **2010,** *81*, 075319.

30. Liu, H. T.; Zhang, Y. M.; Wang, C.; Glazer, J. N.; Shan, Z. Q.; Liu, N. A. Understanding and Controlling the Nucleation and Growth of Zn Electrodeposits for Aqueous Zinc-Ion Batteries. *Acs Appl Mater Inter* **2021,** *13*, 32930-32936.

31. Leistner, K.; Duschek, K.; Zehner, J.; Yang, M.; Petr, A.; Nielsch, K.; Kavanagh, K. L. Role of Hydrogen Evolution during Epitaxial Electrodeposition of Fe on GaAs. *J. Electrochem. Soc.* **2018,** *165*, H3076-H3079.

32. Donahue, M. J.; Porter, D. G. *OOMMF User's Guide, Version 1.0, Interagency Report NISTIR 6376*; National Institute of Standards and Technology: Gaithersburg, MD, 1999.

33. Rave, W.; Fabian, K.; Hubert, A. Magnetic States of Small Cubic Particles with Uniaxial Anisotropy. *J. Magn. Magn. Mater.* **1998,** *190*, 332-348.

34. Landau, L. D.; Lifshitz, E. M. On the Theory of the Dispersion of Magnetic Permeability in Ferromagnetic Bodies. *Phys. Zeitsch. der Sow.* **1935,** *8*, 153-169.

35. Necas, D.; Klapetek, P.; Neu, V.; Havlicek, M.; Puttock, R.; Kazakova, O.; Hu, X.; Zajickova, L. Determination of Tip Transfer Function for Quantitative MFM Using Frequency Domain Filtering and Least Squares Method. *Sci. Rep.* **2019,** *9*, 3880.

36. Hu, X.; Dai, G.; Sievers, S.; Fernández-Scarioni, A.; Corte-León, H.; Puttock, R.; Barton, C.; Kazakova, O.; Ulvr, M.; Klapetek, P.; Havlíček, M.; Nečas, D.; Tang, Y.; Neu, V.; Schumacher, H. W. Round Robin Comparison on Quantitative Nanometer Scale Magnetic Field Measurements by Magnetic Force Microscopy. *J. Magn. Magn. Mater.* **2020,** *511*, 166947.

37. Vock, S.; Hengst, C.; Wolf, M.; Tschulik, K.; Uhlemann, M.; Sasvari, Z.; Makarov, D.; Schmidt, O. G.; Schultz, L.; Neu, V. Magnetic Vortex Observation in FeCo Nanowires by Quantitative Magnetic Force Microscopy. *Appl. Phys. Lett.* **2014,** *105*, 172409.

38. Hug, H. J.; Stiefel, B.; van Schendel, P. J. A.; Moser, A.; Hofer, R.; Martin, S.; Guntherodt, H. J.; Porthun, S.; Abelmann, L.; Lodder, J. C.; Bochi, G.; O'Handley, R. C. Quantitative Magnetic Force Microscopy on Perpendicularly Magnetized Samples. *J. Appl. Phys.* **1998,** *83*, 5609-5620.

39. Sakar, B.; Liu, Y.; Sievers, S.; Neu, V.; Lang, J.; Osterkamp, C.; Markham, M. L.; Öztürk, O.; Jelezko, F.; Schumacher, H. W. Quantum Calibrated Magnetic Force Microscopy. *Phys. Rev. B* **2021,** *104*, 214427.

40. Hu, X. K.; Dai, G. L.; Sievers, S.; Scarioni, A. F.; Neu, V.; Bieler, M.; Schumacher, H. W. Uncertainty Analysis of Stray Field Measurements by Quantitative Magnetic Force Microscopy. *IEEE Trans. Instrum. Meas.* **2020,** *69*, 8187-8195.

41. Lichte, H.; Borrnert, F.; Lenk, A.; Lubk, A.; Roder, F.; Sickmann, J.; Sturm, S.; Vogel, K.; Wolf, D. Electron Holography for Fields in Solids: Problems and Progress. *Ultramicroscopy* **2013,** *134*, 126-134.

42. Midgley, P. A.; Dunin-Borkowski, R. E. Electron Tomography and Holography in Materials Science. *Nat. Mater.* **2009,** *8*, 271-280.

43. Wolf, D.; Biziere, N.; Sturm, S.; Reyes, D.; Wade, T.; Niermann, T.; Krehl, J.; Warot-Fonrose, B.; Büchner, B.; Snoeck, E.; Gatel, C.; Lubk, A. Holographic Vector Field Electron Tomography of Three-Dimensional Nanomagnets. *Commun. Phys.* **2019,** *2*, 87.

44. Aharonov, Y.; Bohm, D. Significance of Electromagnetic Potentials in the Quantum Theory. *Phys. Rev.* **1959,** *115*, 485-491.

45. Bao, Z. L.; Kavanagh, K. L. Aligned Co Nanodiscs by Electrodeposition on GaAs. *J. Cryst. Growth* **2006,** *287*, 514-517.

46. Evans, P.; Scheck, C.; Schad, R.; Zangari, G. Electrodeposition of Epitaxial Nickel Films on GaAs. *J. Magn. Magn. Mater.* **2003,** *260*, 467-472.

47. Bao, Z. L.; Majumder, S.; Talin, A. A.; Arrott, A. S.; Kavanagh, K. L. Epitaxial Fe_xNi_{1-x} Thin Film Contacts to GaAs via Electrochemistry. *J. Electrochem. Soc.* **2008,** *155*, H841-H847.

TOC Graphic

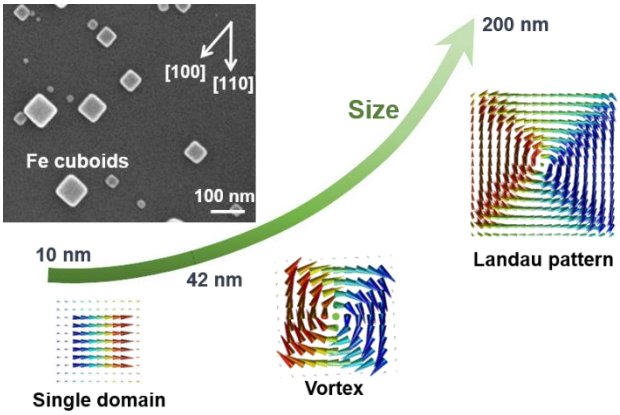
[100]
[110]
Fe cuboids
100 nm
Size
200 nm
10 nm
42 nm
Landau pattern
Vortex
Single domain